AGU PUBLICATIONS

Journal of Geophysical Research: Solid Earth

RESEARCH ARTICLE
10.1002/2015JB011870

Key Points:
- We extract body waves from ambient noise recorded by a dense network
- Two signal-processing filters are applied to retrieve clear body waves
- We use the extracted body waves to estimate 3-D P wave velocities

Correspondence to:
N. Nakata,
nnakata@stanford.edu

Citation:
Nakata, N., J. P. Chang, J. F. Lawrence, and P. Boué (2015), Body wave extraction and tomography at Long Beach, California, with ambient-noise interferometry, *J. Geophys. Res. Solid Earth*, *120*, 1159–1173, doi:10.1002/2015JB011870.

Received 2 JAN 2015
Accepted 23 JAN 2015
Accepted article online 29 JAN 2015
Published online 27 FEB 2015

Body wave extraction and tomography at Long Beach, California, with ambient-noise interferometry

Nori Nakata[1], Jason P. Chang[1], Jesse F. Lawrence[1], and Pierre Boué[1]

[1] Department of Geophysics, Stanford University, Stanford, California, USA

Abstract We retrieve *P* diving waves by applying seismic interferometry to ambient-noise records observed at Long Beach, California, and invert travel times of these waves to estimate 3-D *P* wave velocity structure. The ambient noise is recorded by a 2-D dense and large network, which has about 2500 receivers with 100 m spacing. Compared to surface wave extraction, body wave extraction is a much greater challenge because ambient noise is typically dominated by surface wave energy. For each individual receiver pair, the cross-correlation function obtained from ambient-noise data does not show clear body waves. Although we can reconstruct body waves when we stack correlation functions over all receiver pairs, we need to extract body waves at each receiver pair separately for imaging spatial heterogeneity of subsurface structure. Therefore, we employ two filters after correlation to seek body waves between individual receiver pairs. The first filter is a selection filter based on the similarity between each correlation function and the stacked function. After selecting traces containing stronger body waves, we retain about two million correlation functions (35% of all correlation functions) and successfully preserve most of body wave energy in the retained traces. The second filter is a noise suppression filter to enhance coherent energy (body waves here) and suppress incoherent noise in each trace. After applying these filters, we can reconstruct clear body waves from each virtual source. As an application of using extracted body waves, we estimate 3-D *P* wave velocities from these waves with travel time tomography. This study is the first body wave tomography result obtained from only ambient noise recorded at the ground surface. The velocity structure estimated from body waves has higher resolution than estimated from surface waves.

1. Introduction

Seismic interferometry, one type of cross-correlation analyses, is a powerful tool to extract Earth response from passive data at the local and global scales [e.g., *Curtis et al.*, 2006; *Ruigrok et al.*, 2010; *Nakata and Snieder*, 2011; *Boué et al.*, 2014]. Using this technique, we can extract Green's functions between receivers [*Lobkis and Weaver*, 2001; *Snieder*, 2004; *Wapenaar and Fokkema*, 2006] and reveal velocity and attenuation structures [e.g., *Shapiro et al.*, 2005; *Lin et al.*, 2009; *Lawrence and Prieto*, 2011], as well as monitor subsurface media [e.g., *Brenguier et al.*, 2008; *Mehta et al.*, 2008; *Mainsant et al.*, 2012; *Nakata and Snieder*, 2012]. Although the theory of seismic interferometry is not limited to either body or surface waves [*Aki*, 1957; *Claerbout*, 1968; *Wapenaar*, 2004], surface waves are generally easier to extract with the technique because they dominate the ambient-noise fields.

Despite successes of surface wave extraction, a few studies have found body waves. *Roux et al.* [2005] retrieved *P* direct and Rayleigh waves from ambient noise recorded at Parkfield, California, and separated them in the time-frequency domain. *Draganov et al.* [2009] created a 3-D seismic image using reflected waves obtained from ambient noise and compared it with the image created from active sources. *Nakata et al.* [2011] extracted both surface and body waves from ambient noise, which is mostly traffic-induced noise, and created *S* wave images from reflected waves and inverted *S* velocities from surface waves that correspond well with velocities used for imaging. *Lin et al.* [2013a] observed *P* waves after stacking over all receiver pairs in an array at Long Beach that is adjacent to the one used in this study. *Poli et al.* [2012] found reflected waves from the 410 km and 660 km discontinuities. Reflections at the global scale have also been discovered by averaging correlation functions over many stations [e.g., *Boué et al.*, 2013; *Lin et al.*, 2013b; *Nishida*, 2013]. Assuming homogeneous and isotropic media, *Takagi et al.* [2014] separately obtained body and Rayleigh waves with three-component ambient-noise data. Under the assumption, their technique works well and they successfully extract these waves from observed data, although the assumption is

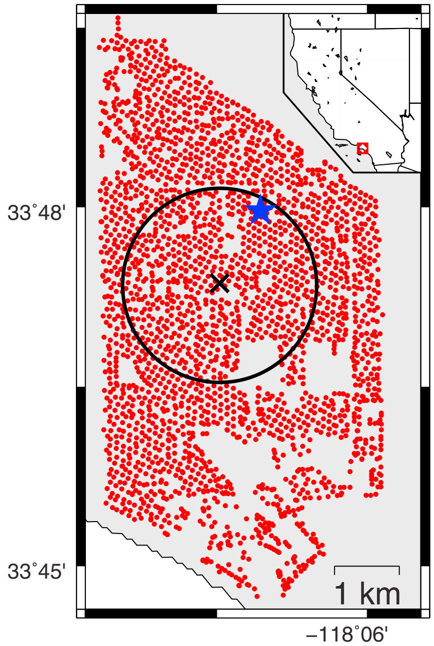

Figure 1. Map of receivers. The red dots show the location of receivers, and the blue star indicates the reference receiver used in Figure 3a. Receivers inside the black circle are used for beamforming analyses in Figure 5. The black cross indicates the central receiver of the black circle. The red square in the inset shows the location of the survey.

strict. In this study, we propose a robust technique to extract body waves from ambient noise even if only one-component data are available.

In this study, we employ signal-processing techniques to improve the quality of retrieved body waves from ambient noise recorded by a dense receiver network at Long Beach, California, USA (Figure 1). The array size is 8.5 $\times$ 4.5 km^2, which is a challenging scale to retrieve body waves since correlation functions computed from ambient noise are contaminated by strong surface waves. Our targets are *P* diving/refracted waves, and the techniques proposed here are designed for extracting these waves. Dense arrays are suitable for ambient-noise tomography, as *Mordret et al.* [2013] and *de Ridder and Biondi* [2013] obtained velocity structures at the reservoir scale with Scholte waves (interface waves between fluid and solid) reconstructed from ambient noise. Using the adjacent array at Long Beach, *Lin et al.* [2013a] revealed 3-D shear-wave velocities from surface wave ambient-noise tomography. However, none of them found prominent body waves from cross-correlation functions without averaging over many stations.

We expect that we can estimate higher-resolution subsurface structure (particularly in depth) by using body waves rather than surface waves because of their higher frequencies and the shapes of their sensitivity kernels [*Dahlen and Baig*, 2002; *Zhou et al.*, 2004]. Thus, in this study, we propose a technique to extract body waves from ambient noise that are suitable for high-resolution *P* wave tomography. We first introduce the data set and initial virtual shot gathers. Then we present signal-processing techniques to extract body waves for the shot gathers. Finally, we invert for 3-D *P* wave velocity structures using travel time tomography with the extracted *P* diving waves and validate the structures as well as estimate the spatial resolution of them using synthetic waveforms.

2. Ambient-Noise Data and Seismic Interferometry

Ambient-noise data were observed by NodalSeismic from January 2012 at Long Beach, California, and continuously recorded ground motion for approximately 3 months. The array is uniquely dense (100 m spacing) and large (2500 receivers) compared with other continuously recording arrays (Figure 1). The receivers are velocity sensors (geophones) with 10 Hz natural frequency and record ground motion in the vertical component only. The receivers are almost evenly distributed over an area of 8.5 $\times$ 4.5 km^2 (with missing sensors in some regions). The sparse receivers in the southeastern region are caused by Alamitos Bay.

Figure 2 shows absolute amplitudes of observed ambient noise at each receiver at different frequencies. The amplitudes are averaged over 2 h of data at 2:00–4:00 P.M. local time on 17 January (Tue) 2012. The amplitudes at the lowest frequency (Figure 2a) are more homogeneous over the array than at higher frequencies. The stronger amplitudes in the south region are related to oceanic noise from the coastline. In Figure 2b (4.0 Hz), strong energy is concentrated around the highway (Interstate 405) and around the bay in the southeast region of the map; and in Figure 2c (10.0 Hz), the highway and local roads generate strongest vibrations. The strong amplitudes in the northwest in Figure 2c are located around the Long Beach Airport.

In this study, we use 10 days of data recorded by all available receivers. We will demonstrate that the 10 day data are enough to extract clear body waves for this survey. First, we downsample the data from 0.002 s sampling to 0.03 s sampling to reduce the computational cost and focus on body waves up to 15 Hz. We

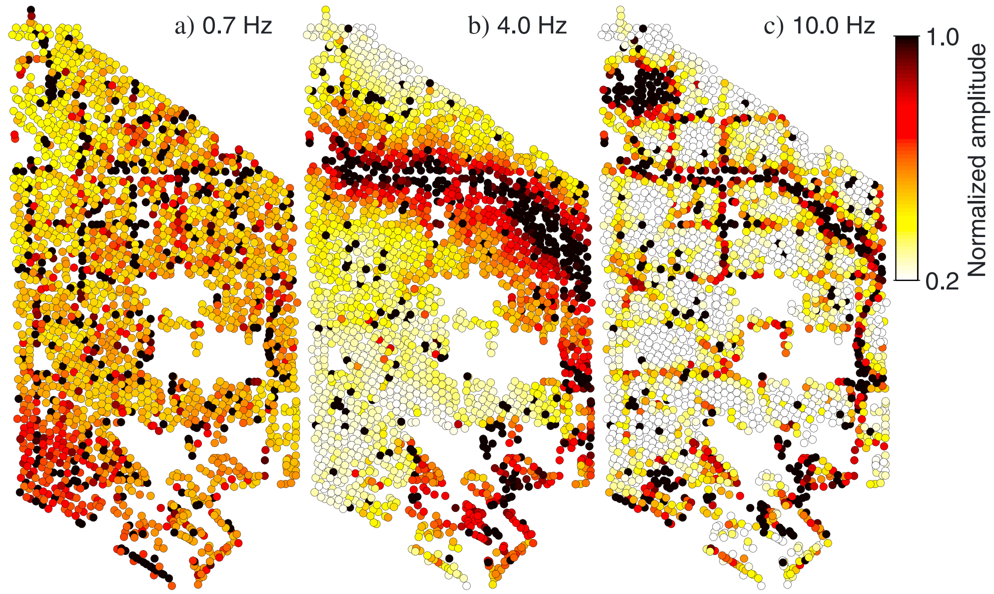

Figure 2. Absolute amplitude of observed ambient noise averaged over 2 h (2:00–4:00 P.M. local time on 17 January (Tue) 2012) in narrow-frequency bands centered at (a) 0.7, (b) 4.0, and (c) 10.0 Hz. Each dot represents each receiver. Amplitudes are normalized at each panel.

then apply seismic interferometry by computing power-normalized cross correlation (cross coherence) between receivers A and B in the frequency domain. This is given by

$$C(B, A, \omega) = \sum_t \frac{u_t(B, \omega) u_t^*(A, \omega)}{|u_t(B, \omega)||u_t(A, \omega)| + \epsilon \langle |u_t(A, \omega)||u_t(B, \omega)| \rangle}, \quad (1)$$

where $u_t(A, \omega)$ is an ambient-noise record in the frequency domain ω observed at receiver A at time interval t, ϵ a regularization parameter [*Nakata et al.*, 2013], $\langle \cdots \rangle$ the ensemble average, and $*$ a complex conjugate. *Nakata et al.* [2011] show that the power normalization is important for retrieving clear propagating waves between receivers A and B from ambient noise and that cross coherence provides the phase of the approximated Green's function. In this study, we use $\epsilon = 0.01$, which is the smallest value needed to overcome the potential instability of $C(B, A, \omega)$ introduced by the division in equation (1). The length of the time interval (t in equation (1)) is 30 min, and the time windows overlap each other by 75%. We sum 30 min correlation functions over 24 h to create daily correlation. When we use a sufficient amount of data, $C(B, A)$ represents wave propagation from receiver A to receiver B, which means A becomes a virtual source. Therefore, by computing equation (1), we can extract surface and/or body waves propagating between two receivers from ambient noise. Figure 3a shows an example of shot gathers of $C(B, A)$, in which A is one receiver (the blue star in Figure 1) and B all other receivers. To plot the virtual shot gather, we average daily correlation functions over 10 days and sort the traces by offset between the virtual source and each receiver (not depending on azimuth). In Figure 3a, although we can reconstruct surface waves with apparent wave speeds between 0.4 and 0.9 km/s, we cannot find clear coherent signals faster than 1.5 km/s (i.e., P waves). The reason why only surface waves are visible in Figure 3a is that surface wave energy dominates the observed ambient-noise data, but body waves are weak compared with other signals.

In Figure 3b, we combine all virtual source gathers to enhance the signal-to-noise ratio (SNR) of body waves. We stack correlated waveforms over all receiver pairs into 50 m offset bins. The number of daily correlations in each bin is shown by the gray line in Figure 4, which indicates that we stack over a tremendous number of daily correlations to construct each trace in Figure 3b. In contrast, only 10 daily correlations are averaged to plot each trace in Figure 3a. In Figure 3b, we obtain clear body waves that propagate faster than 1.5 km/s (as expected from *Lin et al.* [2013a]). Because the wave starts propagating at roughly zero time and because the apparent velocity of the wave increases with further offsets, we assume that this reconstructed wave is a P diving wave. Note that S wave velocities shallower than 1.0 km depth are much slower than 1.5 km/s at the survey area [*Dahlke et al.*, 2014], and hence the obtained waves are not S diving waves. In

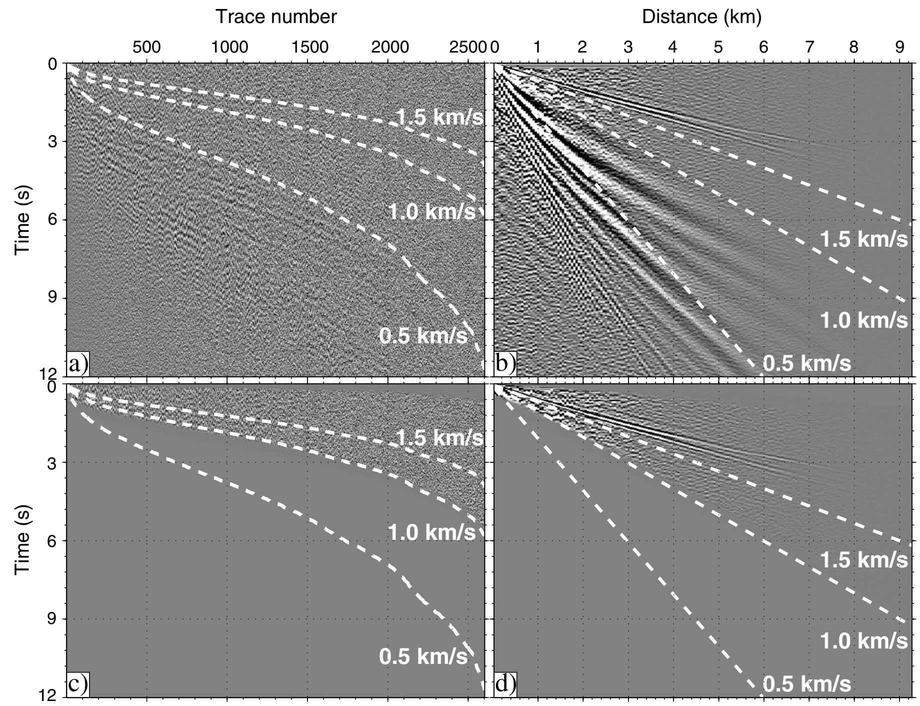

Figure 3. (a) Example of virtual shot gathers constructed from 10 days of ambient-noise data. The virtual source is at the blue star in Figure 1. Trace numbers are sorted by distance from the virtual source. Note that the distance between each trace pair is not constant. The frequency range is from 0.5 to 15.0 Hz. (b) Binning-stacked cross-correlation gather over all virtual shot gathers based on offsets of receiver pairs. The size of each bin for this spatial stacking is 50 m. The frequency range is the same as Figure 3a. (c, d) Shot gathers shown in Figures 3a and 3b, respectively, after applying Gaussian-shape time windows. Signals slower than 1.1 km/s and faster than 6.0 km/s are muted by the windows. The white dashed lines in all panels indicate travel times with constant velocities with an assumption of straight raypaths.

this study, we use the term "diving wave" instead of "refracted wave." Readers can consider diving waves as being continuously refracted due to velocity contrasts. As we show later, the survey region does not have the sharp velocity contrast needed to produce clear critical refraction.

Figure 5a shows the amplitude spectra of the stacked correlation functions shown in Figure 3b in the frequency-wave number (FK) domain after computing a double Fourier transform. Between 2 and 4 Hz, the fundamental and first higher modes of surface waves propagate faster and slower than 2.0 s/km, respectively. Body waves propagate with much faster velocities and the frequency contents of these waves are mostly higher than 3 Hz. In Figures 5b–5g, we beamform correlation functions based on the plane-wave assumption (Bartlett spectral estimation) [*Johnson and Dudgeon*, 1993]. The locations of high amplitudes indicate propagating directions of strong coherent plane waves and their horizontal slownesses. For beamforming, we use correlation functions between the receiver at the black cross and all receivers inside the black circle in Figure 1; therefore, we beamform the coherent energy of ambient noise between receivers. At 1.0 Hz, strong surface waves come from south-southwest, and then the direction

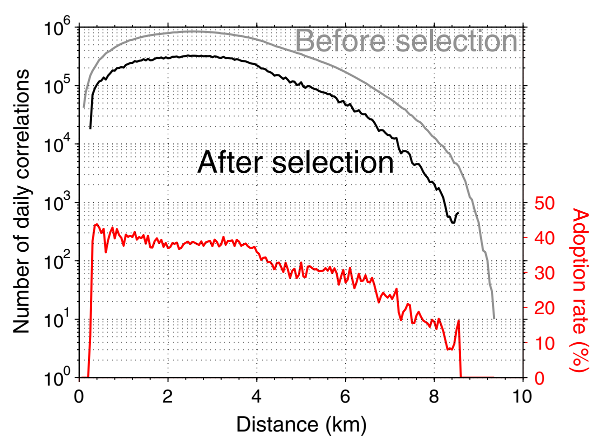

Figure 4. Number of traces before (gray) and after (black) the selection filter based on second correlation at each bin. The gray line shows the number of traces stacked for Figure 3b. The red line (right axis) illustrates the adoption rate of selected traces.

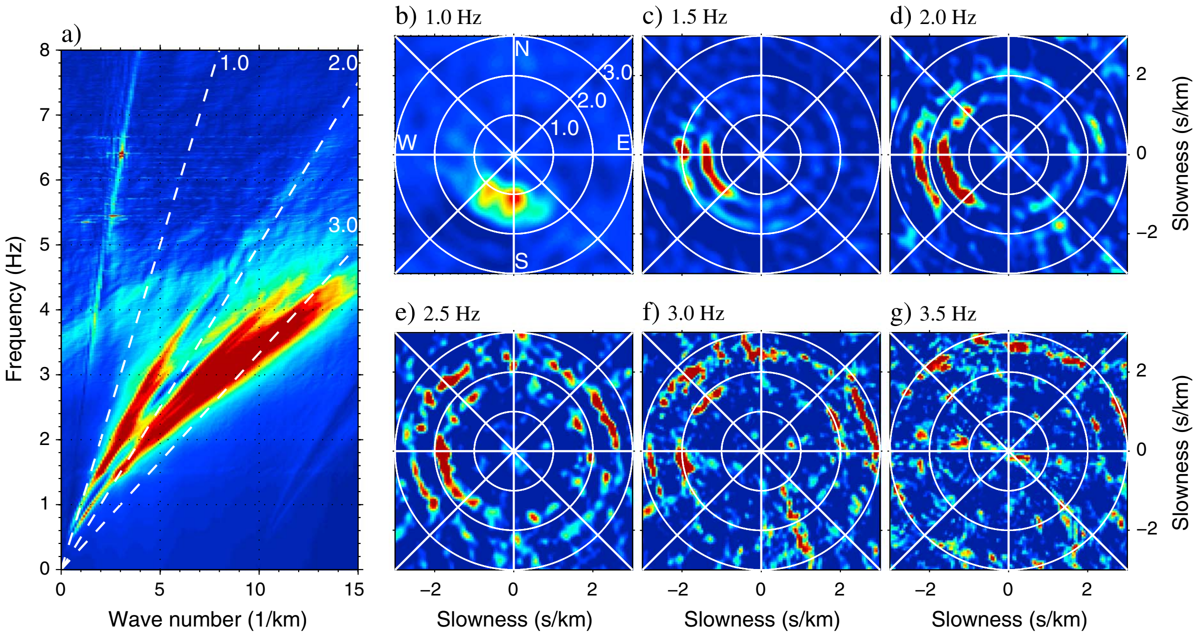

Figure 5. (a) FK amplitude spectra computed from the stacked cross-correlation gather (Figure 3b). The dashed white lines show the constant horizontal slownesses, and the unit of the label of each line is s/km. (b–g) Amplitude spectra in the horizontal slowness domain at each frequency computed by beamforming based on plane-wave projection. The wave number is equivalent to the slowness multiplied by the angular frequency. The frequency on the top of each panel shows the center frequency, and the spectra are averaged over ±0.06 Hz around the center frequency. The white circles show constant slownesses (see Figure 5b). Amplitude spectra in Figures 5b–5g are obtained from the wavefields, which are computed by the cross correlation between the receiver shown by the black cross in Figure 1 and all other receivers inside the black circle in the same figure. Therefore, the direction of waves illustrated in Figures 5b–5g is the direction of incoming waves from the receiver highlighted by the black cross in Figure 1 (see Figure 5b). Warm colors represent high amplitudes.

shifts to west at higher frequencies. In Figures 5c and 5d, two prominent waves propagate from the same direction, which also indicates that these waves are the fundamental and first higher modes. Although the dominant direction is west in Figure 5d, energy comes from a variety of directions (see the bright rings around 1.5 s/km). In Figure 5e, although two rings related to different modes are still observed, the spectra are contaminated by spatial aliasing, which becomes stronger with higher frequencies (Figures 5f and 5g). Strong energy comes from the Long Beach airport (northwest) and the highway (north-northwest) in Figure 5g. Because their aliases exist inside the 1.0 s/km circle, we cannot find clear body wave energy from beamforming analyses.

Although this observation of body waves in Figure 3b is interesting, we cannot yet directly use the waves for tomography studies to estimate 3-D velocity structure because the waves in Figure 3b have poor spatial information. Thus, we use stacked correlation functions as a reference to retrieve body waves between each pair of receivers.

3. Retrieval of Body Waves

For obtaining high-resolution spatial information of the subsurface, we need to extract body waves between each pair of receivers (i.e., from individual virtual shot gathers such as the gather in Figure 3a). We employ two steps to isolate body waves contained within the individual cross-correlation functions.

3.1. Selection Filter

First, we select daily correlation functions which contain relatively strong body wave energy. For the selection filter, we use daily correlation functions instead of 10 day functions because we want to retain as many receiver pairs as possible. For this selection, we use body waves in Figure 3b as a reference. After computing equation (1) and obtaining daily correlation functions, we can roughly approximate the arrival times of diving *P* waves. To isolate body waves and mute surface waves, we apply a time window with Gaussian-shape tapers to each daily correlation and stacked correlation to suppress signals slower than 1.1 km/s and faster than 6.0 km/s (Figures 3c, 3d, and 6a). We then compute a second cross correlation between each daily correlation in Figure 3c and the corresponding trace in the bin of the appropriate

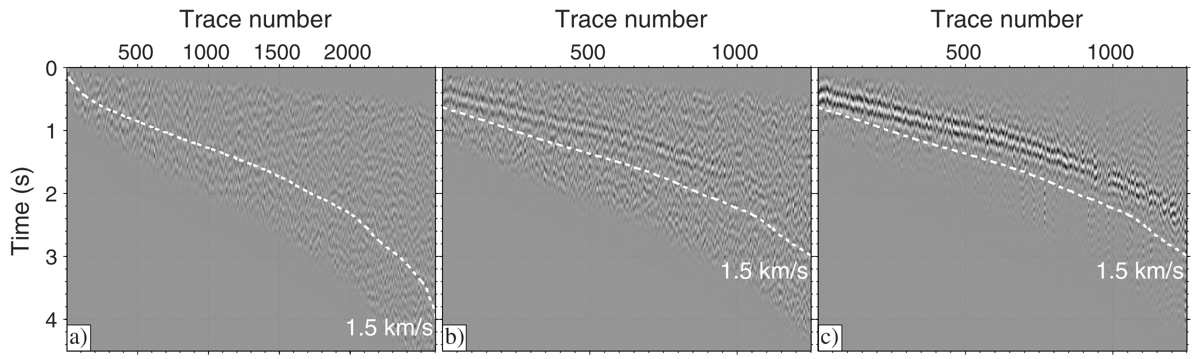

Figure 6. The same virtual shot gather as in Figure 3c after applying a (a) bandpass filter, (b) trace selection, and the (c) noise suppression filter. Note that the time interval for this figure is different from Figure 3c. The frequency range for all panels is from 3.0 to 15.0 Hz. The white dashed line shows the arrival time of a traveling wave with the apparent velocity of 1.5 km/s. The number of traces reduces after the trace selection.

distance in Figure 3d. If the maximum value of the second-correlation function is larger than 0.5, we keep the daily correlation. The value of 0.5 is subjectively determined based on trial and error with this data set. To seek the maximum value, we use not only zero time lags but also all time lags of second-correlation functions because the maximum values may not be at zero lag due to lateral heterogeneity of velocities. After this procedure, we retain about 35% of traces (Figure 4), all of which include strong body waves.

Figure 7 shows stacked waveforms over all retained and discarded correlation functions at a bin of distance 3.0 ± 0.025 km. As shown in Figure 3b, most of the body wave energy is concentrated in a time interval of 1.3–1.9 s. To confirm that we can successfully isolate the traces with strong body wave energy with the second correlation, we compute SNR, which is defined as the average RMS amplitudes between 1.3 and 1.9 s divided by the average RMS amplitudes between 0.0 and 4.5 s; SNR for the retained trace in Figure 7 is 3.3, and that for the discarded trace is 1.3. Therefore, we can identify traces with coherent body wave energy based on the second correlation. The discarded trace in Figure 7 still has body wave energy in 1.3–1.9 s, but the SNR of these body waves before stacking is too small to use. In Appendix A, we show that this selection filter does not introduce biases for travel times of body waves.

Figure 6b shows the virtual shot gather after applying the selection filter to the gather in Figure 6a. Although the number of traces reduces after applying this filter, we retain body waves propagating faster than 1.5 km/s. With this filter, the body waves become more coherent over the traces. For display purposes, we average multiple daily correlation functions at each receiver pair in Figure 6b, but we apply the following noise suppression filter to daily correlation functions without averaging.

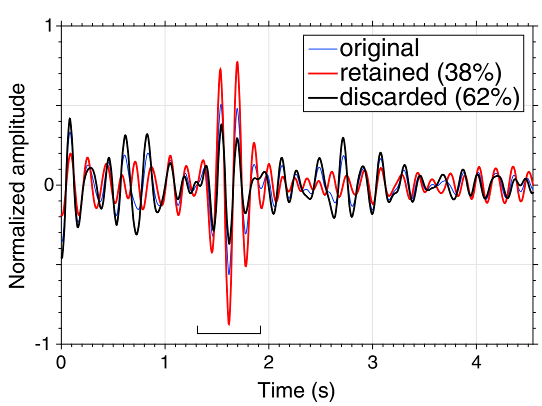

Figure 7. Stacked waveforms over all (original; blue), retained (red), and discarded (black) cross-correlation functions after the selection filter at a bin of distance 3.0 ± 0.025 km. In this bin, retained traces are about 38% of all traces (see Figure 4). The frequency range is from 3.0 to 15.0 Hz. The amplitudes are normalized by the energy of each waveform and have no unit because of the power normalization in equation (1). The target time interval for body waves is around 1.3–1.9 s (highlighted by the black horizontal line).

3.2. Noise Suppression Filter

We further improve the SNR of body waves by using a noise suppression filter. This second step involves an adaptive covariance filter (ACF), which is designed for ambient-noise analysis. It extracts coherent energy and suppresses unwanted noise from correlation functions while assuming that the target signals are coherent and noise is incoherent. In the selection filter, we seek the maximum correlation values across all time lags. Therefore, in each bin, body waves of the selected correlation functions at one time lag are coherent over all traces (i.e., body waves arrive almost the same time). Then we apply the ACF to traces at each time lag in each bin to improve the SNR of body waves for tomography. The ACF measures the coherent energy between all trace

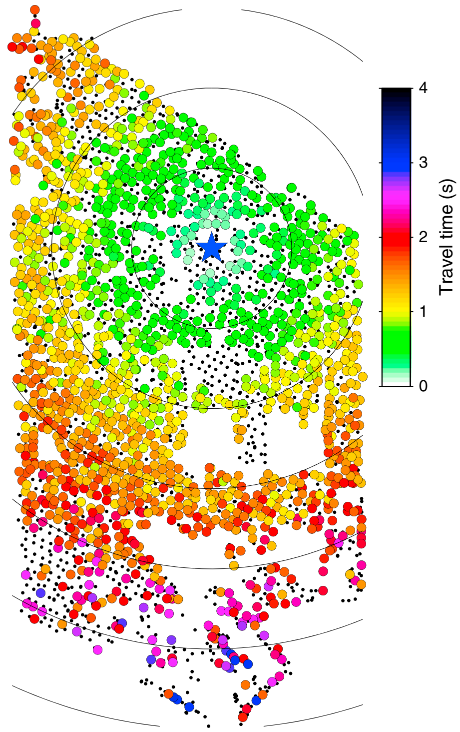

Figure 8. Travel times obtained from the virtual shot gather in Figure 6c. The blue star indicates the location of the virtual source and each dot the location of receivers. The black dots represent receivers which are discarded during the trace selection for this virtual source. The black circles show distance (every kilometer) from the virtual source.

pairs and suppresses incoherent power in each trace. The filter uses $N(N-1)/2$ relative comparison rather than N observations, which yields results with higher SNR. In Appendix B, we detail the construction of the filter.

Figure 6c shows the virtual shot gather after applying the two filters, and we now find clear *P* diving waves. The diving wave propagates with a velocity of approximately 2.0 km/s, and, as we expect, the apparent velocity increases with distance from the virtual source. Note that each trace in Figure 6c is computed from a single receiver pair, and we successfully retrieve body waves between individual pairs. By repeating these processing steps, we can extract body waves propagating from each virtual source. One can use these body waves for any kind of imaging and monitoring purposes. Here we apply travel time tomography to estimate 3-D *P* wave velocity structure.

3.3. Travel Time of Body Waves

We pick the arrival times of *P* diving waves from Figure 6 and show them in map view in Figure 8. Our picks are based on the positive peak amplitude of waves rather than the first break. Because we do not compute a time derivative in equation 1 to extract Green's function, the virtual source is a delta function in space and time. Therefore, the peak amplitude of correlation functions indicates the arrival times. Even when we consider a finite frequency bandwidth, the time of the peak amplitudes of the waves still corresponds to the arrival times of the waves. Although for most of traces we can simply choose the time of the maximum amplitude of *P* diving waves to find the arrival times, some traces have strong side lobes due to the effects of the finite frequency bandwidth. Therefore, we also visually compare waveforms at nearby stations to find accurate arrival times. For stations that have larger than 4 km offset, we observe two *P* diving waves (see Figure 3b; we explain about these waves below), and we choose the arrival times of the faster diving waves.

In Figure 8, the locations of the colored dots show the spatial distribution of retained traces, and the locations of the black dots show the distribution of discarded traces. Figure 8 indicates that the retained traces have no obvious directionality, which means body waves come from a wide range of azimuths. Because we use amplitude-normalized cross correlation (equation (1)) and ACF, relative amplitudes of extracted body waves in Figure 6c may not be the same as the azimuthal strength of original body waves. Although finding the source of the body waves is beyond the scope of this study, we speculate that the source is cultural noise distributed everywhere inside and outside the array. In the next section, we apply travel time tomography to picked arrival times to estimate *P* wave velocities.

4. Body Wave Tomography

After we extract body waves from each virtual shot gather and estimate arrival times for these waves, we have about two million travel times. With these travel times, we implement body wave tomography based on *Hole* [1992]. For the tomography, the grid size is 25 m × 25 m × 25 m, and the size of the model space is 6 km (Easting) × 11 km (Northing) × 1.5 km (depth). Figure 9 shows vertical and horizontal slices of the inverted 3-D *P* wave velocity structure. Because we do not have any information about the velocities at the survey area, we first construct a simple starting model, which linearly increase from 1.5 km/s at the surface to 3.0 km/s at 1.5 km depth, and update the 1-D velocity model during the iteration.

After several iterations (6–13 iterations), we laterally average inverted velocities and construct a new starting 1-D velocity model. Then we start the next iteration with the new starting model to avoid falling into a

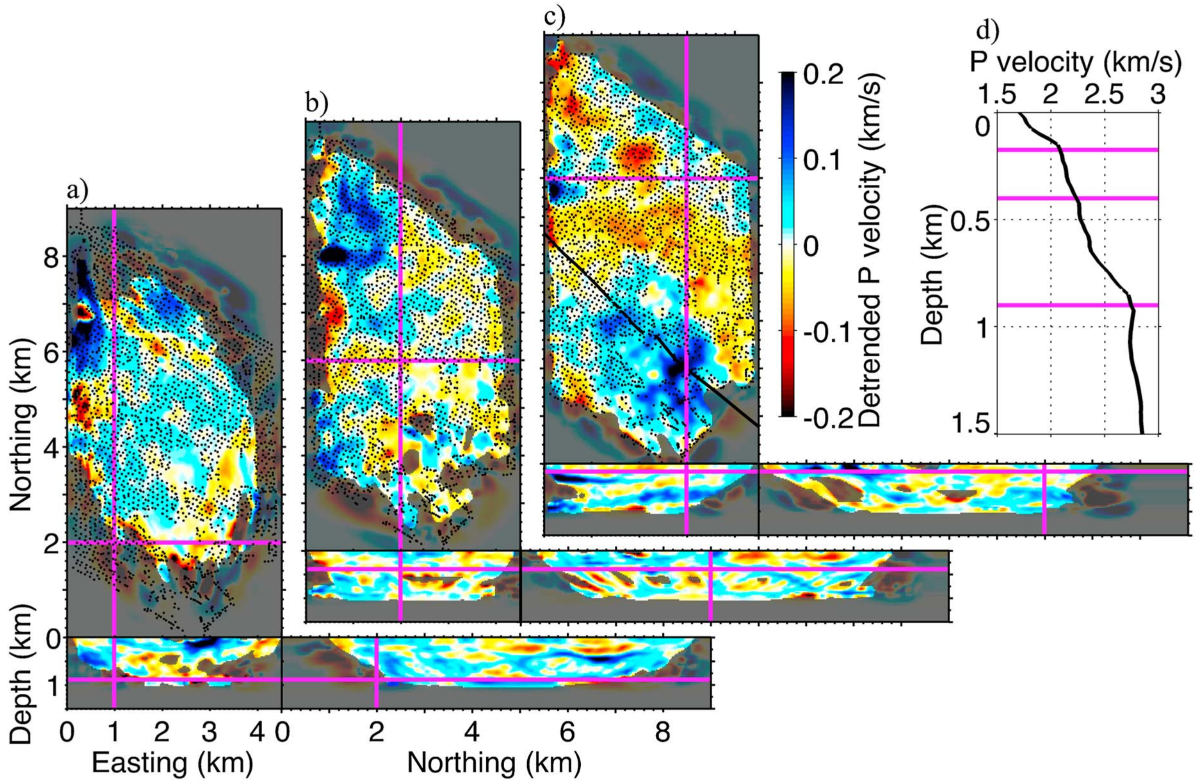

Figure 9. Vertical and horizontal slices of inverted *P* wave velocity cube. (a–c) Slices shift shallower, east, and north. The magenta lines show the location of slices, and the depths of horizontal slices are 0.17, 0.40, and 0.90 km. (d) Velocities are detrended by subtracting the horizontally averaged 1-D velocities. The color map is valid for Figures 9a–9c, where blue indicates velocities faster than the velocity at the corresponding depth in Figure 9d. The shaded areas in the velocity slices are poor ray coverage areas (see Figure C1). The black lines in Figure 9c show the portions of the surface location of the Newport-Inglewood fault [*U.S. Geological Survey and California Geological Survey*, 2006]. The origin of the local coordinate in this figure (Easting = 0 km and Northing = 0 km) is the southwest corner in Figure 1.

local minimum in the model space. Figure 10a shows average RMS errors. When we update the 1-D model (at iterations 6, 16, 29, 42, and 55), the RMS error increases. After the 1-D velocity model converges, we update lateral velocity heterogeneities. Figures 9a–9c show *P* velocity perturbations relative to the best fit 1-D velocity (Figure 9d). To obtain stable velocities, we smooth the inverted velocities with a 3-D Gaussian function at each iteration. The size of the smoothing operator changes during iterations, and the final size (used in Figure 9) is 5 cells × 5 cells × 3 cells. The total raypaths used in Figure 9 is 1,896,663, and the number of rays in each cell is shown in Figure C1. Based on the ray coverages, diving waves reach down to 1.1 km depth (the largest offset we can find body waves is 8.6 km).

Figure 10a shows that we reduce the RMS errors during iterations. Based on the inverted velocities in Figure 9, we compute RMS errors between synthetic and observed travel times at each station (Figure 10b). The RMS errors are averaged over all raypaths at each station. At the edge of the array and the regions where receivers are sparse, the errors are relatively large. Overall, the errors are around 2–3%, which is small enough to interpret lateral and vertical velocity heterogeneities in Figure 9.

The high velocity anomaly in the south region in the horizontal slice of Figure 9c can be related to the Newport-Inglewood fault (the black line in Figure 9c), as imaged from surface waves [*Lin et al.*, 2013a; *Dahlke et al.*, 2014]. The fault is not very obvious in the other horizontal slices, which is caused by the complexities of the fault zone. Based on the 2010 Geologic map of California (http://www.quake.ca.gov), the fault at our survey area is concealed by younger rocks. Based on *Shaw et al.* [2002], we speculate that the northwestern high velocity zone at the depth of 400–500 m (e.g., see the horizontal slice in Figure 9b) corresponds to the top of the base Quaternary surface. Our velocity cube is reasonably consistent with results from an active survey, and we find similar velocity structures especially in the north part of the survey (D. Hollis and M. Padgett, personal communication, 2014).

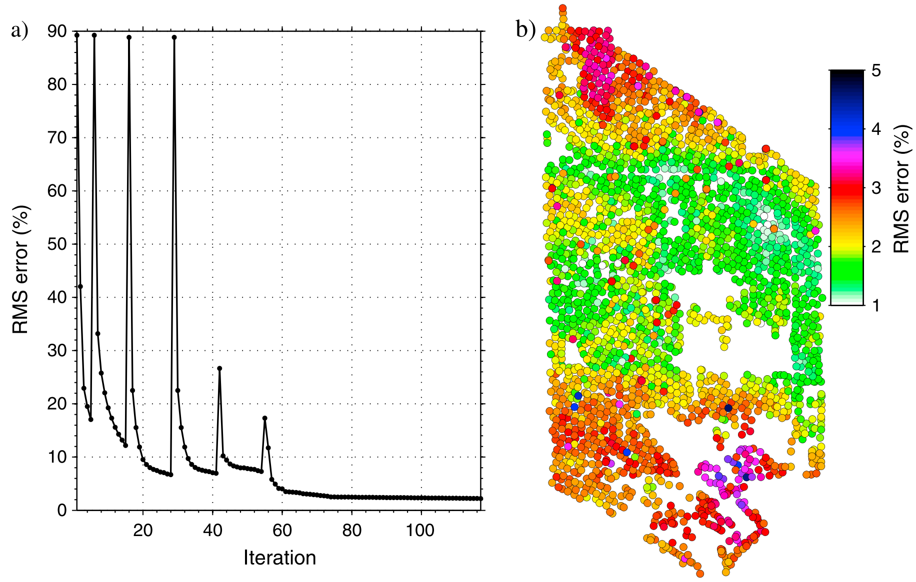

Figure 10. (a) RMS errors at each iteration. The RMS error is the mean of deviations of all travel times from observed travel times (e.g., Figure 8). The deviations are normalized by the observed travel times ($|t_{syn} - t_{obs}|/t_{obs}$, where t_{syn} and t_{obs} are synthesized and observed travel times, respectively). We update the 1-D velocity model at iterations 6, 16, 29, 42, and 55. (b) Final RMS error of travel times at each station. The travel times used for the RMS error is computed from the velocity model in Figure 9 from the observed travel times (e.g., Figure 8).

Dahlke et al. [2014] also find the northwestern high velocity zone using surface wave tomography, but their high velocity zone is much lower resolution than the structure shown in Figure 9. Also, the high velocities around the fault are not obvious. Note that by using body waves, we obtain spatially higher resolution velocity structure compared with surface wave tomography [e.g., *Lin et al.*, 2013a; *Dahlke et al.*, 2014]. To assess the spatial resolution better, Appendix C shows the checkerboard tests. We successfully reproduce checkers with the size of 500 m × 500 m × 250 m.

To estimate the reliability of the velocity model in another way, in Figure 11, we compare the synthetic wavefields obtained from the inverted 1-D velocity model (Figure 9d) with the stacked cross-correlation gather (Figure 3b). We compute the synthetic wavefields using 2-D finite-difference acoustic wave modeling with the laterally constant velocity model given by the 1-D *P* wave velocities (Figure 9d). Compared with the observed wavefields (Figure 11a), we can reconstruct similar synthetic waves (Figure 11b). Waves (1)–(3) in Figure 11b are identical to those in Figure 11a. Although the arrival times of waves (1) and (2) in Figure 11b are almost the same as the times in Figure 11a, the times of wave (3) are slightly later in the synthetic wavefields, which is probably caused by the relatively poor resolution of the diving-wave tomography in the near surface (down to 75 m). According to the synthetic waves, wave (3) is the trapped wave in the near surface (down to 75 m), wave (2) propagates down to the depth of 0.6 km, and wave (1) travels deeper than 0.9 km at far offsets. These similarities of waveforms emphasize the reliability of our inverted velocity model. In addition, the similarities between the synthetic and observed wavefields indicate that we can apply some waveform inversions [e.g., *Luo and Schuster*, 1991; *Kamei et al.*, 2012] to the extracted body waves to estimate even higher-resolution velocities.

Furthermore, this synthetic test explains the kinks of the stacked wavefields (highlighted by (4) and (5) in Figure 11). We apply a velocity filter in the FK domain to wavefields in Figure 3b to isolate waves that propagate with velocities between 2.3–7.0 km/s (Figure 11c). The filtered wavefields can be separated into three parts: waves before (4), between (4) and (5), and after (5). Compared with the travel times of theoretical reflected waves (the blue and red lines in Figure 11d), these three parts are related to the waves propagating at depths shallower than 0.6 km, between 0.6 and 0.9 km, and deeper than 0.9 km, respectively. We calculate RMS velocities [*Yilmaz*, 2001] to estimate the theoretical travel times. Because of the existence of multiple waves and the mild velocity contrasts at 0.6 km and 0.9 km, the reflected waves are difficult to identify, especially at the near offset.

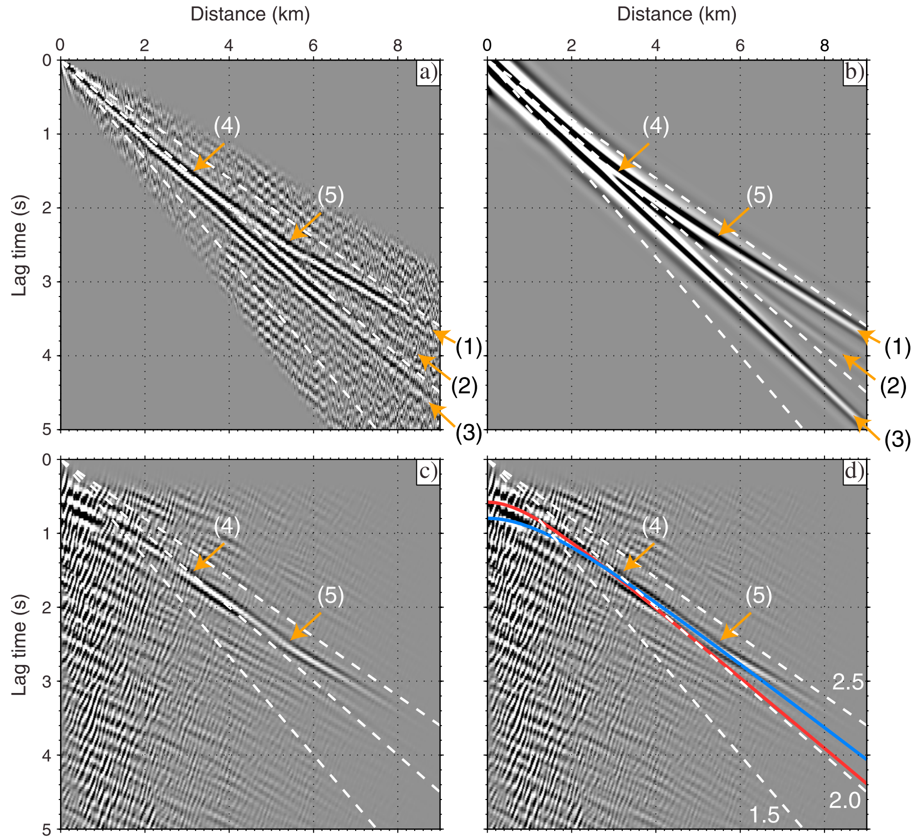

Figure 11. (a) Bandpassed (3.0–10.0 Hz) and time-windowed cross-correlation functions after Figure 3b. The time windows mute signals traveling slower than 1.3 km/s and faster than 3.0 km/s. (b) Synthetic wavefields computed by 2-D finite-difference acoustic wave modeling with the velocity model shown in Figure 9d. (c) Bandpassed (3.0–10.0 Hz) and velocity-passed (2.3–7.0 km/s) cross-correlation functions after Figure 3b. To mute the noise around zero time lag, Gaussian-shape filters are applied. (d) Annotated figures after Figure 11c. The red and blue lines indicate the arrival times of reflected waves from the interface at depths of 0.6 km and 0.9 km, respectively (Figure 9d). Three white lines in all panels show arrival times of waves with constant velocities of 2.5, 2.0, and 1.5 km/s (Figure 11d). Each arrow highlights waves which are discussed in the main text.

5. Conclusions

We retrieve body waves which propagate between single pairs of receivers from ambient noise recorded by a local-scale dense array. To extract body waves, we use two steps of signal processing: selection of traces based on maximum absolute values of the second correlation and the noise suppression filter (ACF). With this technique, each trace in virtual shot gathers clearly shows *P* diving waves. We discard more than half of all correlation functions, and we successfully retain body wave energy at about two million pairs of receivers. Because we use the stacked waveforms over all virtual sources as a reference to seek body waves, we need to reconstruct clear body waves in the stacked waveforms. Therefore, dense receiver arrays are suitable for this technique, but one can apply it to any array since the proposed technique is robust across all survey areas and scales.

After extracting body waves, we apply travel time tomography to estimate 3-D velocity structure, which is the first *P* wave velocity structure with reasonably high resolution obtained from ambient noise observed at the free surface. The usage of body waves is not limited to travel time tomography. Since we preserve the waveforms of body waves during the procedure proposed here, waveform inversions are also interesting to apply. Due to the dense network, rays cover the entire area well, and we can invert 3-D velocity structures with sufficiently small RMS errors. The velocities obtained from body waves are much higher resolution than those from surface waves. This process is one type of target-oriented seismic interferometry and is useful for estimating high-resolution velocity structure and imaging.

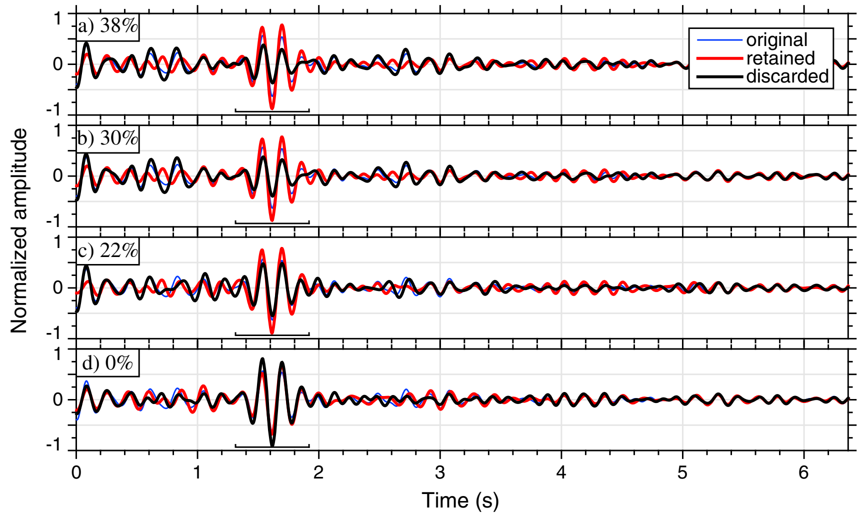

Figure A1. Stacked waveforms using different reference traces for second cross correlation; (a) the trace used in Figure 7, (b) same as Figure A1a with 0.24 s time shift, (c) stacked trace over all traces in a bin at 4.0 ± 0.025 km, and (d) band-limited white noise. The frequency range is the same as Figure 7. The percentages on the top left are the ratio of retained traces. The blue lines are the same for all panels.

Appendix A: Robustness of the Selection Filter

To confirm that our second cross correlation correctly retains traces without biases, we perform several tests. For the second correlation, we need a reference waveform. In the main text, we use the binning-stacked waveforms as a reference (Figures 7 and A1a), and in this Appendix, we employ other reference waveforms to show the robustness of the selection filter.

First, we use the same stacked waveforms as used in Figure A1a, but we apply 0.24 s time shifts. If the arrival time of body waves in the retained traces computed with the time-shifted waveform is also shifted, the selection filter introduces a bias to extract body waves. Figure A1b shows, however, that we can extract almost the same body waves as shown in Figure A1a without any time shifts. Because we use the reference which is not the most suitable one, the number of retained traces reduces (38% → 30%). When we use the binning-stacked trace at 4.0 km instead of at 3.0 km, we can still isolate body wave energy (Figure A1c) due to the similarity between the traces at 3.0 km and 4.0 km. The quality of the filter reduces, and we can find only 60% of traces compared to Figure A1a. When we use band-limited white noise as a reference, very few traces are selected and we cannot isolate any body wave energy as expected (Figure A1d).

From these tests, we find almost no time shifts of body waves in retained traces. Therefore, we confirm that we do not introduce any biases caused by the selection filter and successfully retain traces containing stronger body waves.

Appendix B: Adaptive Covariance Filter

The adaptive covariance filter (ACF) is a noise suppression filter that enhances coherent signals over all traces. This filter is not limited to extracting body waves, as we can also use it for finding surface waves. Here we introduce the ACF with an example. Figure B1a shows the wavefields after the selection process (at time lag of the maximum value of the second correlation 0.00 ± 0.015 s and bin 3.00 ± 0.025 km). By applying seismic interferometry to ambient noise, we try to extract coherent energy between two stations. The coherent energy is, for example, related to surface and/or body waves propagating between two stations. Because the coherent energy is usually weak, we average cross-correlation functions over long time periods or many station pairs (mean stacking). For example, we can average over all traces in Figure B1a to enhance body waves around 1.6 s. Instead of mean stacking, we suppress incoherent noise using ACF to avoid averaging over many station pairs, which reduces spatial resolution (e.g., Figure 3).

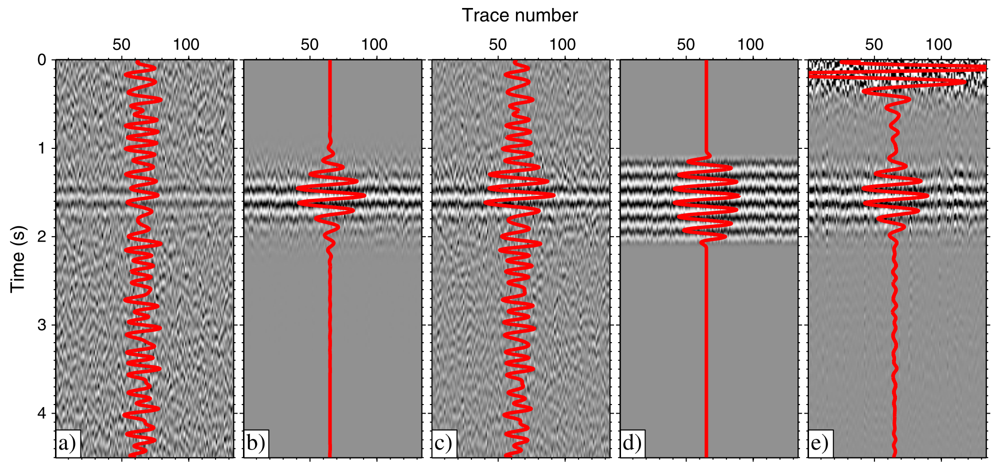

Figure B1. Example of noise suppression filters. (a) Prefilter and (b–d) adaptive covariance filtered wavefields at a bin of distance 3.0 ± 0.025 km with the same time lag (time lag is equal to zero) for the second cross correlation. We use 0.9 s time windows with 90% overlap for all panels, and harshnesses are $g = 1.5$ (Figure B1b), $g = 0.2$ (Figure B1c), and $g = 10$ (Figure B1d). (e) Wavefields shown in Figure B1a after applying the adaptive polarization filter (0.9 s time windows with 90% overlap and $g = 2.0$). The red trace depicts the waveforms at trace number 65.

The ACF is based on the adaptive polarization filter [*Samson and Olson*, 1981; *Du et al.*, 2000] and suppresses noise that is not coherent over a data set. Data sets contain multiple time series obtained from different time intervals or station pairs. When $x_i(t)$ represents i^{th} time series (each trace in Figure B1a), the filtered signals ($x_i'(t)$) are given by [*Samson and Olson*, 1981; *Du et al.*, 2000]

$$x_i'(t) = \frac{1}{2\pi}\int_{-\infty}^{\infty} p^g(\omega)x_i(\omega)e^{i\omega t}\mathrm{d}\omega, \tag{B1}$$

where $x_i(\omega) = \int_{-\infty}^{\infty} x_i(t)e^{-i\omega t}\mathrm{d}t$, $p(\omega)$ is the filter, and g is a positive number that adjusts the filter harshness. To obtain $p(\omega)$, we first compute a cross-spectrum matrix,

$$S_{ij}(\omega) = x_i(\omega)x_j^*(\omega), \tag{B2}$$

where $*$ is the complex conjugate. The matrix $S_{ij}(\omega)$ is equivalent to the temporal covariance matrix. At each frequency, the filter is given by

$$p(\omega) = \frac{\sum_i^N\sum_j^N S_{ij}(\omega) - \sum_i^N S_{ii}(\omega)}{(N-1)\sum_i^N S_{ii}(\omega)}, \tag{B3}$$

where N is the number of total traces ($N = 135$ in Figure B1). When the observations are completely dissimilar, $\sum_i^N\sum_j^N S_{ij}(\omega) = \sum_i^N S_{ii}$ and $p(\omega) = 0$. If the observations are identical, $\sum_i^N\sum_j^N S_{ij}(\omega) = N\sum_i^N S_{ii}$ and $p(\omega) = 1$. Therefore, $p(\omega)$ is between 0 and 1, and represents the coherency among traces. Because the filter $p(\omega)$ is independently constructed at each frequency, we can suppress both broadband and narrowband noise by using the ACF.

Following the suggestion of *Samson and Olson* [1981], we apply running time windows to wavefields and separately apply the filter at each time window. Due to the short-time windows, the ACF is sensitive to temporally localized noise. To avoid truncation errors, we apply a Hanning taper at each short-time window.

Figure B1b shows the same wavefields as shown in Figure B1a after ACF with the best parameters, which are chosen by trial and error based on a visual inspection. The ACF has three parameters (length of time windows, overlap of time windows, and the harshness), and here we choose 0.9 s windows, 90% overlap, and $g = 1.5$. The length should be short enough to isolate temporal noise but long enough to preserve low-frequency signals. More overlaps make outputs less sensitive to the starting and ending samples of time windows [*Welch*, 1967]. When g is small, incoherent noise has a higher chance to pass the filter (Figure B1c), and when g is large, the filtered signals are strangely normalized (Figure B1d) or the wavefields sometimes become discontinuous.

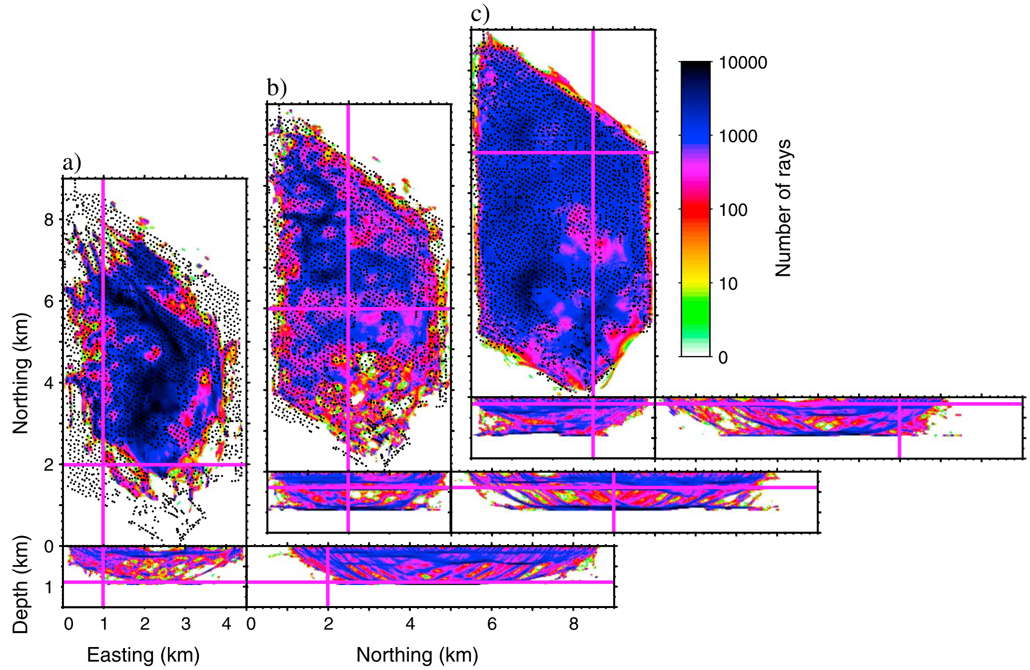

Figure C1. Number of rays at each cell for the travel time tomography without smoothing. The locations of horizontal and vertical slices are the same as those in Figure 9.

The filter (equation B3) is slightly different from the polarization filter, $p(\omega)=\left\{Ntr\left[\mathbf{S}^2(\omega)\right]-(tr\left[\mathbf{S}(\omega)\right])^2\right\}/\left\{(N-1)\,(tr\left[\mathbf{S}(\omega)\right])^2\right\}$, where $\mathbf{S}(\omega)$ is the matrix form of equation (B2) and *tr* is the trace of matrix [*Samson and Olson*, 1981]. Our filter more severely damps frequencies that exhibit the most scatter. In Figure B1e, we show the wavefields after applying the adaptive polarization filter with the best parameters (0.9 s window, 90% overlap, and $g=2.0$) [*Samson and Olson*, 1981; *Du et al.*, 2000]. The polarization filter also enhances the body wave signals (1–2 s in Figure B1e), but the signal-to-noise ratio is lower than the covariance filter (compare the amplitudes of noise after 3 s in Figures B1b and B1e). The strong amplitudes around time 0 s are caused by inaccurate determination of the variance [*Du et al.*, 2000].

Appendix C: Ray Coverage and Checkerboard Test

Figure C1 shows the number of rays in each cell for the tomography in Figure 9. Note that we do not apply any smoothing to show the numbers in Figure C1, and for tomography, we use a 3-D Gaussian function for smoothing (5 cells × 5 cells × 3 cells). At the center of the survey area, we have good ray coverage, even at the deepest horizontal slice.

We conduct 3-D checkerboard tests to assess the resolution of our travel time tomography. We add spatial sinusoidal velocity perturbations (maximum 5%) to our final 3-D velocity model (Figure 9). Two sizes of checkers are employed for the tests: 500 m × 500 m × 250 m (Figure C2a) and 800 m × 800 m × 400 m (Figure C2b). We estimate the travel times between each receiver pair for the velocity model with perturbations using the forward modeling used for the tomography, and then invert velocities using the velocity model shown in Figure 9 as a starting model. To take into account the errors of the travel time estimation in the real data, we add random travel time errors after the forward modeling. Based on the RMS errors in Figure 10, we use random errors based on a normal distribution with standard deviation of 2% travel time at each receiver pair.

Figures C2c and C2d show the inverted velocity perturbations for the small and large checkers, respectively. We reproduce well the patterns of checkers in the almost entire unshaded areas. Therefore, the resolution of our tomography is at most 500 m in the horizontal direction and 250 m in the vertical direction down to 1.1 km depth at the center of the survey. Some reproduced checkers at the edges of the survey area in Figure C2c are resolved well in one direction due to the directionality of the majority of raypaths (e.g., at

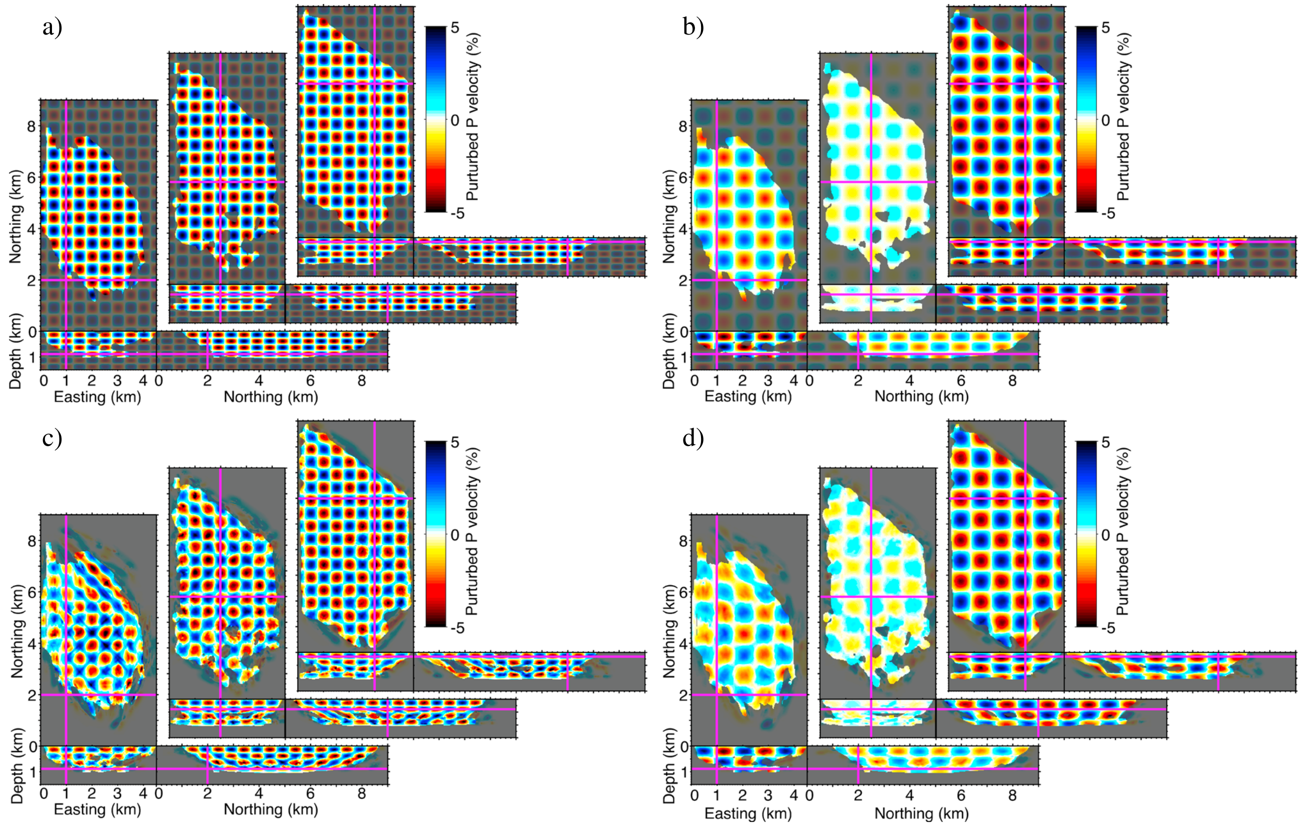

Figure C2. (a, b) Checkers for checkerboard tests and (c, d) their inverted results. The size of checkers in Figures C2a and C2c) is 500 m × 500 m × 250 m, and that in Figures C2b and C2d) is 800 m × 800 m × 400 m. The background velocity is the inverted *P* wave velocity cube (Figure 9), and the maximum velocity perturbation is 5%. The locations of horizontal and vertical slices and the shaded areas for all panels are the same as those in Figure 9.

the northeast corner of the deepest horizontal slice). Note that checkers in Figure C2d are less directional. With these tests, we confirm that we have high resolution for inverting *P* wave velocities using the extracted body waves.

Acknowledgments
We are grateful to Signal Hill Petroleum, Inc. for access to this data set. Readers should directly ask Signal Hill Petroleum for the data set. We also thank Mike Padgett at Signal Hill Petroleum, Dan Hollis at NodalSeismic, John A. Hole at Virginia Tech, and Biondo Biondi at Stanford University for their professional help and comments. We are grateful to Super Micro Computer, Inc. for providing computer resources and Andy Kim at Supermicro for his support. Nori Nakata appreciates financial support of the George Thompson Fellowship at Stanford University, and Jason P. Chang thanks to the sponsors of the Stanford Exploration Project for their support. Figure 1 is produced by using the Generic Mapping Tools (GMT).

References

Aki, K. (1957), Space and time spectra of stationary stochastic waves, with special reference to microtremors, *Bull. Earthquake Res. Inst. Tokyo*, *35*, 415–456.

Boué, P., P. Poli, M. C. C. Pedersen, X. Briand, and P. Roux (2013), Teleseismic correlations of ambient seismic noise for deep global imaging of the Earth, *Geophys. J. Int.*, *194*, 844–848.

Boué, P., P. Poli, M. Campillo, and P. Roux (2014), Reverberations, coda waves and ambient noise: Correlations at the global scale and retrieval of the deep phases, *Earth Planet. Sci. Lett.*, *391*, 137–145.

Brenguier, F., M. Campillo, C. Hadziioannou, N. M. Shapiro, R. M. Nadeau, and E. Larose (2008), Postseismic relaxation along the San Andreas Fault at Parkfield from continuous seismological observations, *Science*, *321*, 1478–1481.

Claerbout, J. F. (1968), Synthesis of a layered medium from its acoustic transmission response, *Geophysics*, *33*(2), 264–269.

Curtis, A., P. Gerstoft, H. Sato, R. Snieder, and K. Wapenaar (2006), Seismic interferometry—Turning noise into signal, *Leading Edge*, *25*(9), 1082–1092.

Dahlen, F. A., and A. M. Baig (2002), Fréchet kernels for body-wave amplitudes, *Geophys. J. Int.*, *150*, 440–466.

Dahlke, T., G. Beroza, and J. Chang (2014), Stochastic variability of velocity estimates using eikonal tomography on the Long Beach data set, SEG Expanded Abstracts 2014 presented at SEG Annual Meeting, 26-31 October, Denver, Colorado, USA, 2352–2456.

de Ridder, S. A. L., and B. L. Biondi (2013), Daily reservoir-scale subsurface monitoring using ambient seismic noise, *Geophys. Res. Lett.*, *40*, 2969–2974, doi:10.1002/grl.50594.

Draganov, D., X. Campman, J. Thorbecke, A. Verdel, and K. Wapenaar (2009), Reflection images from ambient seismic noise, *Geophysics*, *74*(5), A63–A67.

Du, Z., G. R. Foulger, and W. Mao (2000), Noise reduction for broad-band, three-component seismograms using data-adaptive polarization filters, *Geophys. J. Int.*, *141*, 820–828.

Hole, J. A. (1992), Nonlinear high-resolution three-dimensional seismic travel time tomography, *J. Geophys. Res.*, *97*, 6553–6562.

Johnson, D. H., and D. E. Dudgeon (1993), *Array Signal Processing: Concepts and Techniques*, Englewood Cliffs, N. J.

Kamei, R., R. G. Pratt, and T. Tsuji (2012), Waveform tomography imaging of a megasplay fault system in the seismogenic Nankai subduction zone, *Earth Planet. Sci. Lett.*, *317–318*, 343–353, doi:10.1016/j.epsl.2011.10.042.

Lawrence, J. F., and G. A. Prieto (2011), Attenuation tomography of the western United States from ambient seismic noise, *J. Geophys. Res.*, *116*, B06302, doi:10.1029/2010JB007836.

Lin, F.-C., M. H. Ritzwoller, and R. Snieder (2009), Eikonal tomography: Surface wave tomography by phase front tracking across a regional broad-band seismic array, *Geophys. J. Int.*, *177*, 1091–1110, doi:10.1111/j.1365-246X.2009.04105.x.

Lin, F.-C., D. Li, R. W. Clayton, and D. Hollis (2013a), High-resolution 3D shallow crustal structure in Long Beach, California: Application of ambient noise tomography on a dense seismic array, *Geophysics*, *78*, Q45–Q56.

Lin, F.-C., V. C. Tsai, B. Schmandt, Z. Duputel, and Z. Zhan (2013b), Extracting seismic core phases with array interferometry, *Geophys. Res. Lett.*, *40*, 1049–1053, doi:10.1002/grl.50237.

Lobkis, O. I., and R. L. Weaver (2001), On the emergence of the Green's function in the correlations of a diffuse field, *J. Acoust. Soc. Am.*, *110*(6), 3011–3017.

Luo, Y., and G. T. Schuster (1991), Wave-equation traveltime inversion, *Geophysics*, *56*(5), 645–653.

Mainsant, G., E. Larose, C. Brönnimann, D. Jongmans, C. Michoud, and M. Jaboyedoff (2012), Ambient seismic noise monitoring of a clay landslide: Toward failure prediction, *J. Geophys. Res.*, *117*, F01030, doi:10.1029/2011JF002159.

Mehta, K., J. L. Sheiman, R. Snieder, and R. Calvert (2008), Strengthening the virtual-source method for time-lapse monitoring, *Geophysics*, *73*(3), S73–S80.

Mordret, A., M. Landès, N. M. S. C. Singh, P. Roux, and O. I. Barkved (2013), Near-surface study at the Valhall oil field from ambient noise surface wave tomography, *Geophys. J. Int.*, *193*, 1627–1643.

Nakata, N., and R. Snieder (2011), Near-surface weakening in Japan after the 2011 Tohoku-Oki earthquake, *Geophys. Res. Lett.*, *38*, L17302, doi:10.1029/2011GL048800.

Nakata, N., and R. Snieder (2012), Estimating near-surface shear-wave velocities in Japan by applying seismic interferometry to KiK-net data, *J. Geophys. Res.*, *117*, B01308, doi:10.1029/2011JB008595.

Nakata, N., R. Snieder, T. Tsuji, K. Larner, and T. Matsuoka (2011), Shear-wave imaging from traffic noise using seismic interferometry by cross-coherence, *Geophysics*, *76*(6), SA97–SA106, doi:10.1190/GEO2010-0188.1.

Nakata, N., R. Snieder, S. Kuroda, S. Ito, T. Aizawa, and T. Kunimi (2013), Monitoring a building using deconvolution interferometry. I: Earthquake-data analysis, *Bull. Seismol. Soc. Am.*, *103*(3), 1662–1678, doi:10.1785/0120120291.

Nishida, K. (2013), Global propagation of body waves revealed by cross-correlation analysis of seismic hum, *Geophys. Res. Lett.*, *40*, 1691–1696, doi:10.1002/grl.50269.

Poli, P., M. Campillo, H. Pedersen, and L. W. Group (2012), Body-wave imaging of Earth's mantle discontinuities from ambient seismic noise, *Science*, *338*, 1063–1065.

Roux, P., K. Sabra, P. Gerstoft, and W. Kuperman (2005), P-waves from cross correlation of seismic noise, *Geophys. Res. Lett.*, *32*, L19303, doi:10.1029/2005GL023803.

Ruigrok, E., X. Campman, D. Draganov, and K. Wapenaar (2010), High-resolution lithospheric imaging with seismic interferometry, *Geophys. J. Int.*, *183*, 339–357, doi:10.1111/j.1365-246X.2010.04724.x.

Samson, J. C., and J. V. Olson (1981), Data-adaptive polarization filters for multichannel geophysical data, *Geophysics*, *46*, 1423–1431.

Shapiro, N. M., M. Campillo, L. Stehly, and M. H. Ritzwoller (2005), High-resolution surface-wave tomography from ambient seismic noise, *Science*, *307*, 1615–1618.

Shaw, J. H., A. Plesch, J. F. Dolan, T. L. Pratt, and P. Fiore (2002), Puente hills blind-thrust sysmtem, Los Angeles, California, *Bull. Seismol. Soc. Am.*, *92*(8), 2946–2960.

Snieder, R. (2004), Extracting the Green's function from the correlation of coda waves: A derivation based on stationary phase, *Phys. Rev. E: Stat. Phys. Plasmas Fluids Relat. Interdisciplin. Top.*, *69*, 046610.

Takagi, R., H. Nakahara, T. Kono, and T. Okada (2014), Separating body and rayleigh waves with cross terms of the cross-correlation tensor of ambient noise, *J. Geophys. Res. Solid Earth*, *119*, 2005–2018, doi:10.1002/2013JB010824.

U.S. Geological Survey, and California Geological Survey (2006), *Quaternary fault and fold database for the United States.* [Available at http://earthquake.usgs.gov/hazards/qfaults/, last accessed November, 2014.]

Wapenaar, K. (2004), Retrieving the elastodynamic Green's function of an arbitrary inhomogeneous medium by cross correlation, *Phys. Rev. Lett.*, *93*, 254301.

Wapenaar, K., and J. Fokkema (2006), Green's function representations for seismic interferometry, *Geophysics*, *71*(4), SI33–SI46.

Welch, P. D. (1967), The use of fast Fourier transform for the estimation of power spectra: A method based on time averaging over short, modified preriodograms, *IEEE Trans. Audio Electroacoust.*, *AU-15*(2), 70–73.

Yilmaz, O. (2001), *Seismic Data Analysis, Investigations in Geophysics*, vol. 10, 2nd ed., Society of Exploration Geophysicists, Tulsa, Okla., doi:10.1190/1.9781560801580.

Zhou, Y., F. A. Dahlen, and G. Nolet (2004), Three-dimensional sensitivity kernels for surface wave observables, *Geophys. J. Int.*, *158*, 142–168.